Layering in shales controls primary migration in source rocks

Thomas Chauve[1], Luc Scholtès[2], Frédéric-Victor Donzé[3], Nazmul Haque Mondol[4], François Renard[1,3]

[1]The Njord Centre, PGP, Department of Geosciences, box 1048, University of Oslo, Blindern, NO-0316 Oslo, Norway
[2]Université de Lorraine, CNRS, GeoRessources, 54500 Vandoeuvre–lès–Nancy, France
[3]Univ. Grenoble Alpes, Univ. Savoie Mont Blanc, CNRS, IRD, IFSTTAR, ISTerre, 38000 Grenoble, France
[4]University of Oslo (UiO), Department of Geosciences, Oslo, Norway and Norwegian Geotechnical Institute (NGI), Oslo, Norway

Key Points:

- Shale permeability increases during primary migration due to microfracturing processes induced by kerogen maturation.
- Elastic properties contrasts between layers cause stress variations that control the propagation of hydraulically driven microfractures.
- Under normal faulting stress, as in the Draupne maturation induced microfractures creates fluid path controlling primary migration.

Corresponding author: François Renard, `francois.renard@geo.uio.no`

Abstract

The process of primary migration, which controls the transfer of hydrocarbons from source to reservoir rocks, necessitates the existence of fluid pathways in formations with inherently low permeability. Primary migration starts with the maturation of organic matter that produces fluids which increase the effective stress locally. The interactions between local fluid production, microfracturing, stress conditions, and transport remain difficult to apprehend in shale source rocks. Here, we analyze these interactions using a coupled hydro-mechanical model based on the discrete element method. The model is used to simulate the effects of fluid production emanating from kerogen patches contained within a shale rock alternating kerogen-poor and kerogen-rich layers. We identify two microfracturing mechanisms that control fluid migration: i) propagation of hydraulically driven fractures induced by kerogen maturation in kerogen-rich layers, and ii) compression induced fracturing in kerogen-poor layers caused by fluid overpressurization of the surrounding kerogen-rich layers. The relative importance of these two mechanisms is discussed considering different elastic properties contrasts between the rock layers, as well as various stress conditions encountered in sedimentary basins, from normal to reverse faulting regimes. Results show that the layering causes local stress redistribution that controls the prevalence of each mechanism over the other. When the vertical stress is higher than the horizontal stress in kerogen-rich layers, microfractures propagate from kerogen patches and rotate toward a direction perpendicular to the layers. Microfracturing in kerogen-poor layers is more pronounced when the confinement in these layers is higher. Those mechanisms were shown to be representative of Draupne formation.

1 Introduction

In several geological systems, fluid may be expelled from low permeability rocks. This process happens during dehydration of sediments and serpentine in subduction zones, dehydration of clay minerals in sedimentary rocks during diagenesis, or hydrocarbon expulsion from source rocks, a process called primary migration. Shale rocks deposited in sedimentary basins can act as source rocks of hydrocarbon-bearing reservoirs and cap rocks for the same reservoirs, or for underground repositories, such as those used for CO_2 storage. Shales prevent fluids to escape due to their low permeability and to a capillary sealing mechanism controlled by small pores (Horsrud et al., 1998). Shale rocks, when acting as source rocks, are of primary interest for hydrocarbon exploration. However, the apparent low permeability of shales questions the mechanisms that lead to hydrocarbon expulsion. Some shales collected in outcrops or cores samples contain microfractures and microporosity at small scales that can increase the overall permeability properties of the rock (Gale et al., 2014; Kalani et al., 2015; Ougier-Simonin et al., 2016). However the mechanisms at the origin of these microfractures remain unclear.

Kerogen maturation into hydrocarbons leads to overpressures that can induce fracture propagation and therefore fluid migration. Such mechanism has been proposed to explain shale microfracturing (Pelet & Tissot, 1971; Vernik, 1994; Jin et al., 2010; Fan et al., 2012) and has been numerically investigated using a coupled hydro-mechanical model by Teixeira et al. (2017). These authors showed that kerogen maturation forms microfractures that tend to propagate toward the main principal stress direction within an initially homogeneous and isotropic material. Under normal faulting conditions encountered in many sedimentary basins, the largest principal stress direction is vertical, thus allowing fluid migration when vertical tensile fractures open along this direction.

Shale rocks are complex materials due to their formation process that involves the successive deposition of millimeter to centimeter thick layers with variable mineral and organic contents. Shales are inherently anisotropic materials (Valès et al., 2004) that show fractal distribution of layer thickness (Li et al., 2017). Such structural layering can lead

to local stress inversion between successive sedimentary units within sedimentary basins (Gunzburger & Magnenet, 2014). Depending on the deposition environment and on the local tectonics, stress conditions can vary from normal faulting stress regime when the vertical stress σ_v is larger than the horizontal stress σ_h, to reverse faulting stress regime when the horizontal stress is larger than the vertical stress (Zoback, 2007, chapter 9) (Zhang & Zhang, 2017). Obviously, the interaction between the far-field stress conditions and the mechanical properties of the materials plays a major role on the deformation processes taking place in shale formations.

We propose here a numerical study to investigate the influence of shale layering on the microfracturing processes occurring during kerogen maturation and the effect of these processes on permeability. Two microfracturing mechanisms are proposed and discussed as candidates to increase the permeability (Figure 1). The first mechanism is the propagation of microfractures emanating from kerogen patches due to the local increase of fluid pressure. The second mechanism is the ability of this overpressure to damage the surrounding rock and the layers that do not contain kerogen. The first mechanism has been discussed in previous studies (e.g. (Jin et al., 2010) and references therein), while, to our knowledge, the second mechanism has not been proposed yet to explain primary migration in source rocks.

The main goal of the present study is thus to quantify the importance of these two different mechanisms on microfracture formation induced by kerogen maturation in layered rocks. In particular, the study focuses on the effect of the mechanical contrast (Young's modulus) between layers on these fracturing mechanisms considering three different mechanical loading conditions: a hydrostatic case ($\sigma_v = \sigma_h$), a normal faulting case (i.e. extension, $\sigma_v > \sigma_h$) and a reverse faulting case (i.e. compression, $\sigma_v < \sigma_h$). Finally, we apply our findings to explain primary migration in the Draupne formation in the Norwegian Continental Shelf.

2 Materials and methods

2.1 Numerical modeling of shale maturation

We implemented numerical models to investigate rock fracturing induced by kerogen maturation. We used the coupled hydro-mechanical (HM) model proposed by Papachristos et al. (2016) to simulate the propagation of microfractures within shale rocks. The model combines the discrete element method (DEM and the pore-scale finite volume method (FVM) implemented in the open source platform YADE DEM (Kozicki & Donzé, 2008, 2009; Šmilauer et al., 2015). The same approach has been previously used to investigate kerogen maturation in an homogeneous isotropic rock by Teixeira et al. (2017). Details of the HM-DEM model can be found in Papachristos et al. (2016). In short, the rock material is modeled as an assembly of bonded rigid particles whose respective motion is ruled by Newton's second law. The poral space is discretized through a Delaunay triangulation that allows to simulate a compressible fluid flow in-between particles. The method is hydro-mechanically coupled in the sense that a deformation of the solid skeleton induces local fluid overpressures and associated flows, while, reciprocally, fluid overpressures induce forces on the solid particles which eventually generates hydraulically driven cracks as a result of inter-particle bond breakage (Figure 2). In the following we use the engineering stress convention where compressive stresses are negative and extensional stresses are positive.

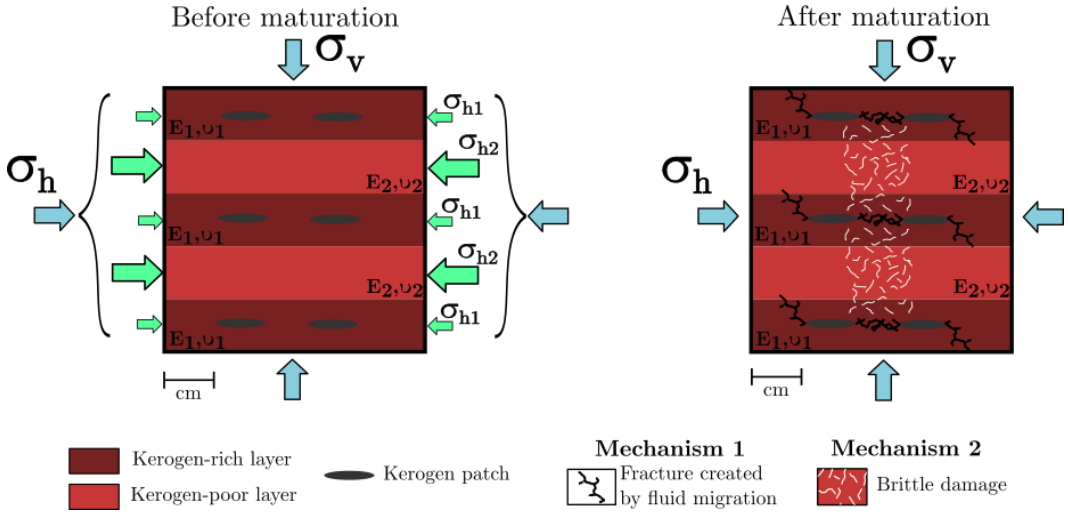

Figure 1. Schematic representation of two fracturing mechanisms responsible for fluid expulsion in tight layered rocks. Left: Schematic shale rock structure before maturation. Right: Microfracturing process during kerogen maturation. The increase of fluid pressure in kerogen patches produces microfractures through two mechanisms. Mechanism 1: nucleation, propagation and rotation of hydraulically driven microfractures emanating from kerogen patches (in black) in layers with high kerogen content (dark red). Mechanism 2: compression induced microfractures (in white) in layers with low kerogen content (light red). Both mechanisms increase the permeability of the medium and may lead to the formation of connected fluid pathways connected, allowing fluid expulsion from a tight rock.

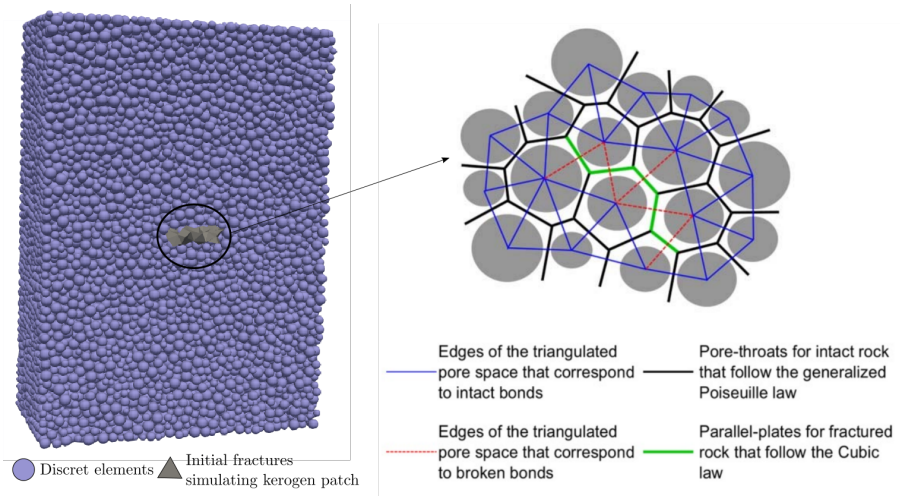

Figure 2. Principle of the numerical model illustrated by 3D and 2D sketches of the bonded particles medium and the microfractures that form between them. Modified from Papachristos et al. (2016).

2.2 Numerical simulation setup

2.2.1 Model geometry

The simulated rock specimen is made of 50,000 spherical particles packed in a volume of dimension $14 \times 10 \times 10\ cm^3$. The medium is divided into 7 horizontal layers, alternating material with high organic content (#1, red) and material with low organic content (#2, blue), as shown in figure 3). The layers with high organic content contain kerogen patches, whereas the layers with low organic content do not. The interfaces between the layers have the same cohesion as between particles withing the layers.

The kerogen patches within high organic content layers are modeled as penny shaped cracks with a radius of 1 cm. Each crack extends over 6.5 discrete elements in the bedding direction of the shale material to reproduce the preferential orientation of kerogen patches observed using synchrotron X-ray tomography imaging (Kobchenko et al., 2011; Panahi et al., 2013, 2018). The number of elements has been set as a compromise between a fine discretization of the layers, with 6.5 discrete elements across the layer thickness, and a reasonable simulation time. Kerogen maturation is simulated by injecting fluid within all penny shaped kerogen-filled cracks at constant flow rate. The fluid has a bulk modulus of $2.2 \times 10^9\ Pa$, a viscosity of $10^{-3}\ Pa.s$.

The injection rate and the simulation time cannot be directly linked to the geological time under which maturation takes place. This choice was made to ensure the simulation to be quasi-static. The elastic waves induced by bond breakages are damped to avoid any dynamic effects. Hence, the rate of fluid production in the kerogen patches defines the time scale and therefore, no absolute time is given when presenting the results of the numerical simulations in the following.

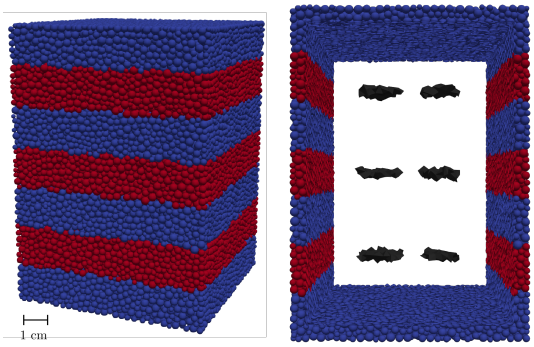

Figure 3. Discrete elements packing used for the numerical simulations. The elements colored in red correspond to material #1, a layer with high organic content. The elements colored in blue correspond to material #2, a layer with low organic content. In dark are shown the initial kerogen patches where fluid pressurization occurs.

2.2.2 Stress boundary conditions

Three sets of numerical experiments were designed to simulate three different states of stresses: hydrostatic conditions ($\sigma_v = \sigma_h = -17.3\ MPa$), normal faulting conditions ($\sigma_v = -30\ MPa, \sigma_h = -11\ MPa$) and reverse faulting conditions ($\sigma_v = -10\ MPa, \sigma_h = -21\ MPa$). The normal faulting conditions are chosen to reproduce the stress conditions measured at depth in the Draupne Shale formation of the Norwegian Continental Shelf (Zadeh et al., 2017). The reverse faulting and hydrostatic stress conditions are de-

fined such that the first invariant of the stress tensor (i.e. the pressure, $I_1 = trace(\bar{\bar{\sigma}})$) is the same for all simulations.

2.2.3 Material properties

Each layer is modeled as an isotropic and impermeable rock material. The mechanical properties are chosen from values measured at depth in the Draupne Shale formation (Mondol, 2019), a major source rock in the North Sea. The Young's modulus and the Poisson's ratio are different for each layer whereas the uniaxial tensile strength are identical. The properties of the high and low organic content layers are summarized in table 1.

Table 1. Mechanical properties of the different layers forming the medium.

	High organic content layer #1, red	Low organic content layer #2, blue
Young's modulus (GPa)	9.9, 8.9, 7.9, 6.8	14.9, 13.2, 11.5, 9.8, 8.0
Poisson's ratio (-)	0.34	0.24
Uniaxial Tensile Strength (MPa)	3.5	3.5

2.3 State of stress in a layered elastic material

The state of stress in a stratified material formed by two series of isotropic layers with different elastic properties can be obtained from Hooke's law:

$$\bar{\bar{\varepsilon}} = \frac{1+\nu}{E}\bar{\bar{\sigma}} - \frac{\nu}{E}trace(\bar{\bar{\sigma}}) \tag{1}$$

We consider here a shale formed by two kinds of layers: kerogen-rich layers contain patches of kerogen, whereas kerogen-poor layers do not contain organic matter (Figure 1). With burial, the organic matter present in the kerogen patches matures, producing hydrocarbons and increasing locally the fluid pressure. This local fluid production may fracture the rock. As the main principal stress direction controls the direction of hydrofracture propagation during kerogen maturation (Teixeira et al., 2017), the ratio σ_{hi}/σ_v between the horizontal stress and the vertical stress in the layer, $\#i$, plays a crucial role. If $\sigma_{hi}/\sigma_v > 1$, the main principal stress direction is horizontal (i.e. parallel to bedding) and if $\sigma_{hi}/\sigma_v < 1$, the principal stress direction is vertical (i.e. perpendicular to bedding). Expression of this ratio is given in equations 2 and 3 for a material made up of two medium, where E_i and nu_i are the elastic parameters of material $\#i$, $P_\sigma = \sigma_h/\sigma_v$ is the ratio between the imposed horizontal stress and vertical stress, and $q1$ is the volume proportion of material #1. A derivation of those expressions is given in Appendix A.

$$\frac{\sigma_{h1}}{\sigma_v} = \frac{E_1 P_\sigma\,(\nu_2 - 1) + (E_1\nu_2 - E2\nu1)\,(1-q1)}{E_1 q_1(\nu_2 - 1) + E2(1-q_1)(\nu_1 - 1)} \tag{2}$$

$$\frac{\sigma_{h2}}{\sigma_v} = \frac{E_2 P_\sigma\,(\nu_1 - 1) + (E_2\nu_1 - E1\nu2)\,q1}{E_1 q_1(\nu_2 - 1) + E2(1-q_1)(\nu_1 - 1)} \tag{3}$$

Figure 4 presents a comparison between the local stress calculated from the analytical solutions (equations 2 and 3), and the local stress predicted by the DEM model

for hydrostatic stress conditions. The model is in good agreement with the analytical solutions for both the local vertical stress σ_v and the local horizontal stress σ_h. The results also show that, depending on the mechanical contrast between the layers, the orientation of the largest principal stress can be either vertical or horizontal in the high organic content layers as observed in some log measurement (Gunzburger & Magnenet, 2014).

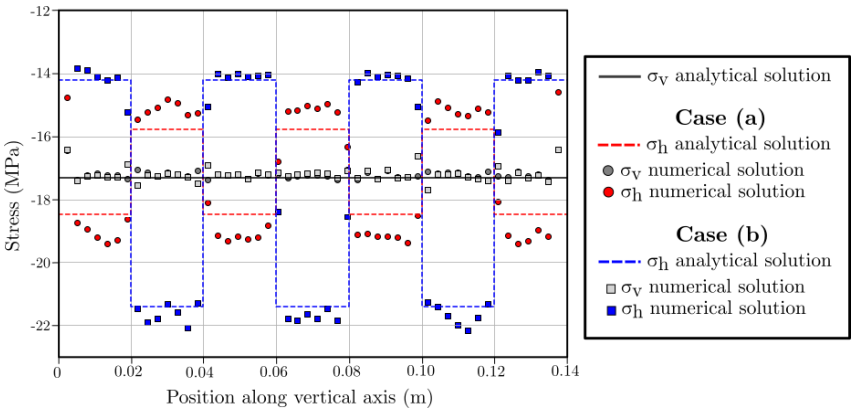

Figure 4. Comparison between theoretical local stresses calculated using equations 2 and 3, and numerical local stresses predicted by the DEM model considering a hydrostatic state of stress. The numerical local stresses are computed through averaging the per particle stresses over a layer of thickness δx along the vertical axis. These results are obtained for two sets of high organic content and low organic content rock parameters under hydrostatic loading conditions ($P_\sigma = 1$) and with $q1 = 3/7$, as shown on figure 3.
(a) Material #1, $E_1 = 6.8\ GPa,\ \nu_1 = 0.34$. Material #2, $E_2 = 14.9\ GPa,\ \nu_2 = 0.24$.
(b) Material #1, $E_1 = 9.9\ GPa,\ \nu_1 = 0.34$. Material #2, $E_2 = 8.0\ GPa,\ \nu_2 = 0.24$.

3 Results for a non-layered rock

The way microfractures initiate and propagate directly depends on the properties of the host medium. Here, we study the effect of each property on the kerogen maturation induced damage in a non-layered medium to identify the microfracturing mechanisms without considering the structural effects caused by the layering. The case of a layered rock is studied in section 4.

3.1 Microfracturing induced by the pressurization of a kerogen patch

We simulate here the maturation of a sample containing a unique kerogen patch subjected to different far field stress regimes (figure 5). The four stress conditions were defined keeping the same value for the first invariant of the stress tensor I_1, and different differential stresses equal to $0, 9, 11.5$ and $19\ GPa$ respectively.

Under hydrostatic loading (differential stress equal to 0), the hydraulically induced fractures are preferentially oriented in the $x0z$ plane, parallel to the bedding, as shown on the fluid pressure map as well as on the stereographic projection of the microfractures orientation distribution. In this case, the direction of microfracture propagation is driven by the orientation of the initial kerogen patch.

For the simulation with the highest differential stress ($19\ GPa$), the hydraulically induced fractures are preferentially oriented in the yOz vertical plane perpendicular to the bedding as confirmed by the stereographic projection of the microfracture planes that

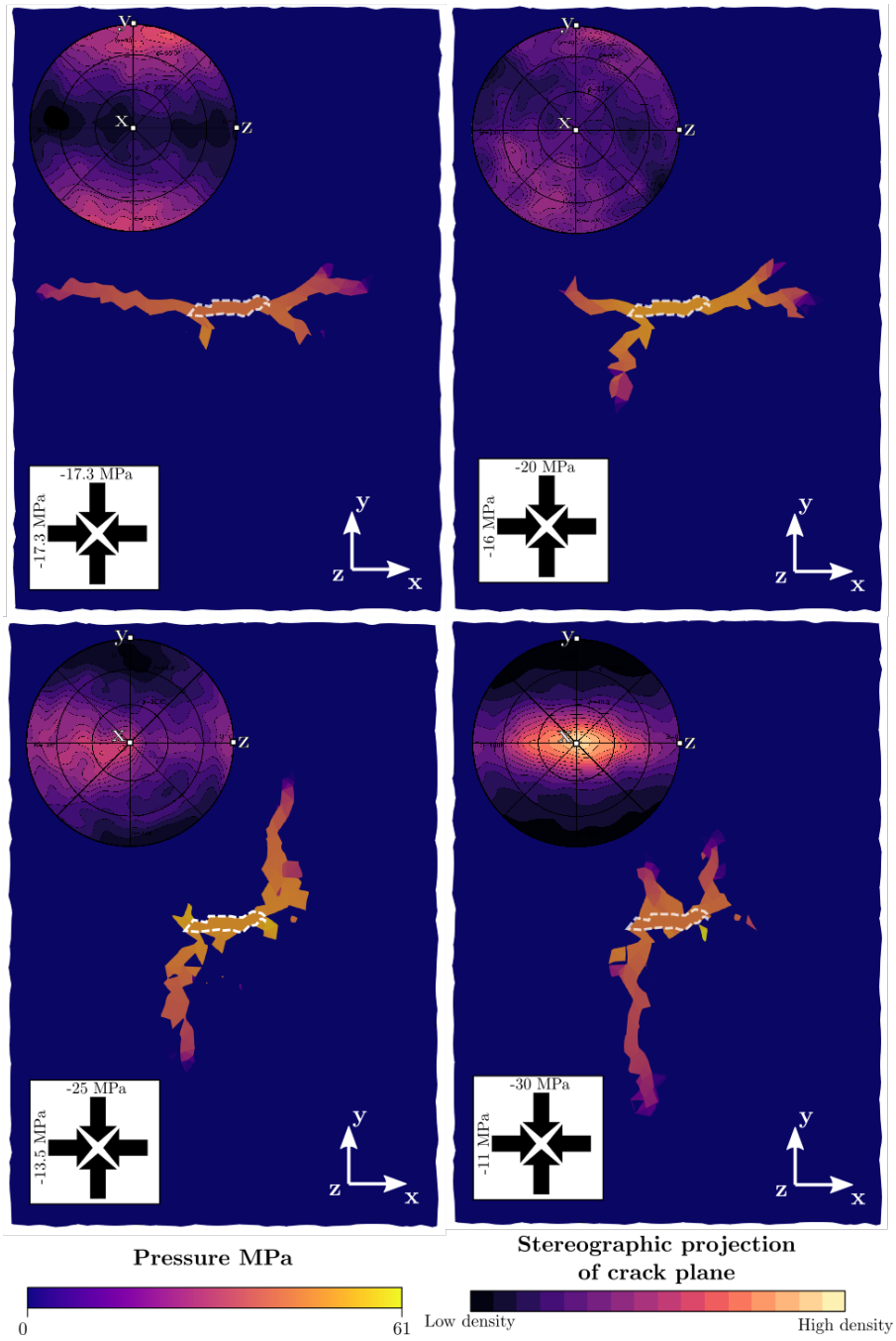

Figure 5. Single kerogen patch maturation under different stress conditions into a homogeneous rock ($E = 9.9\ GPa$). For each imposed stress condition, a cross-section of the fluid pressure field in the middle of the sample is displayed. The applied stress conditions are indicated in the bottom left corner and a stereographic projection of the microfracture planes is displayed as an inset in the top left corner. Four different stress conditions are shown that all have the same first invariant stress tensor, I_1. The initial kerogen patch is indicated with a white dashed contour. All simulations are stopped after the same amount of fluid injected, $V_f = 1\ mm^3$.

shows a maximum in the x direction. This results confirms that fluid induced microfractures propagate and rotate in the direction of the largest principal stress direction, along the y-axis in this case.

Both the stereographic plots and the fluid pressure maps show that an increase of the differential stress in the vertical direction enhances the number of vertical fractures, an effect that can be interpreted by a faster reorientation of the fractures and the creation of multiple vertical fluid pathways, as shown by the differences between the $-25\ MPa$ and $-30\ MPa$ cases on figure 5.

To conclude, for a given set of material properties, an increase of differential stress enhances fracture propagation toward the principal stress direction, which favors the creation of vertical fluid pathways in the medium.

3.2 Overpressures due to kerogen maturation in layers with high organic content

During the maturation of organic matter, the production of fluid in the kerogen patches results in an increase of fluid pressure. This pressure increase in the kerogen-rich layers induces an increase of differential stress in the kerogen-poor layers located below and above them which can lead to the formation of microfractures (Mechanism 2 in Figure 1). In order to assess the effects of material properties and external loading conditions on this mechanism, we performed simulations with one patch in an homogeneous high organic content rock whose Young's modulus is varied between 6.8 and 9.9 GPa (table 1).

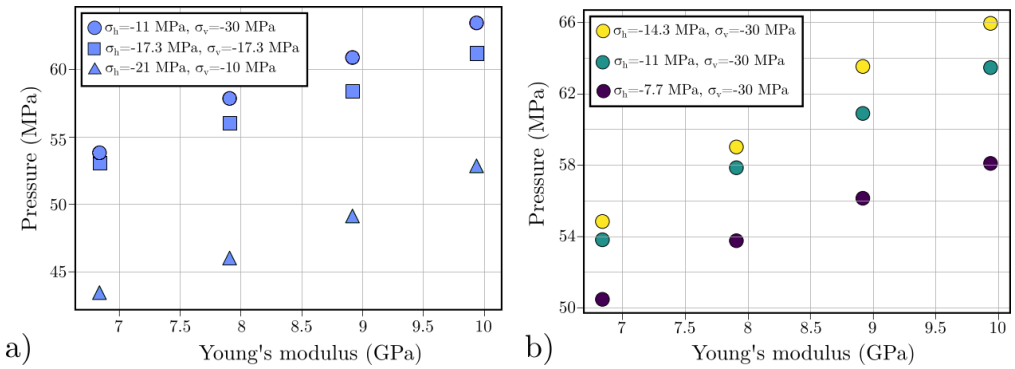

Figure 6. Evolution of the fluid pressure peak during during pressurization of the kerogen patch. *a)* Results for three different stresses conditions. *b)* Result for normal faulting stress condition with different horizontal stresses of $-14.3\ MPa, -11\ MPa, -7.7\ MPa$.

Figure 6*(a)* presents the maximum fluid pressures recorded within the kerogen patch at the onset of propagation for the three different stress conditions: hydrostatic, normal faulting, and reverse faulting stress regimes respectively. The maximum pressure increases with the Young's modulus. This likely results from the fact that fracture propagation is controlled by the stress field at the crack tip which is related by the opening of the crack (the displacement of its lips). Hence, when the Young's modulus increases, a higher pressure is needed to reach the same critical opening. The increase in pressure is also controlled by the normal stress applied on the kerogen patch. In the configurations tested here, this normal stress corresponds to the vertical stress σ_v.

Figure 6*(b)* presents results obtained for three different loading conditions defined with the same vertical stress but different horizontal stresses ranging from $-7.7\ MPa$

to $-14.3\ MPa$. In these configurations, the mean stress in the solid, i.e. the first stress invariant I_1, is therefore different. Results show that the maximum fluid pressure increases with I_1.

To conclude, the maximum fluid pressure within the kerogen patches increases when the Young's modulus, the first stress invariant, or the vertical stress increases.

3.3 Effect of Young's modulus on damage in layers with low organic content

As presented in section 3.2, the maturation of organic matter induces local stress increases around kerogen patches. This stress increase damages rocks layers located in-between kerogen patches (Mechanism 2 shows in figure 1).

In order to assess the dependency of damage on the stress increase and material properties (Young's modulus), we performed triaxial compression test simulations on low organic content rock #2. The initial stress condition corresponds to the normal faulting stress scenario defined such as $\sigma_v = -30\ MPa$ and $\sigma_h = -11\ MPa$. The vertical stress is increased by increment of $1\ MPa$ up to $-40\ MPa$. Figure 7 presents the amount of cracks generated in the medium as a function of the vertical stress considering five different simulations run with different Young's moduli ranging from 6.8 GPa to 9.9 GPa (table 1). In the range of parameter investigated here, the Young's modulus has a negligible effect on the damage produced within the sample. Damage results from the increase of the vertical stress, or, conjointly, from the increase of the first stress invariant I_1.

To conclude, microfracturing in low organic content layers is controlled by the confining pressure in this layer (i.e., the first stress invariant $I_{1,\#2}$).

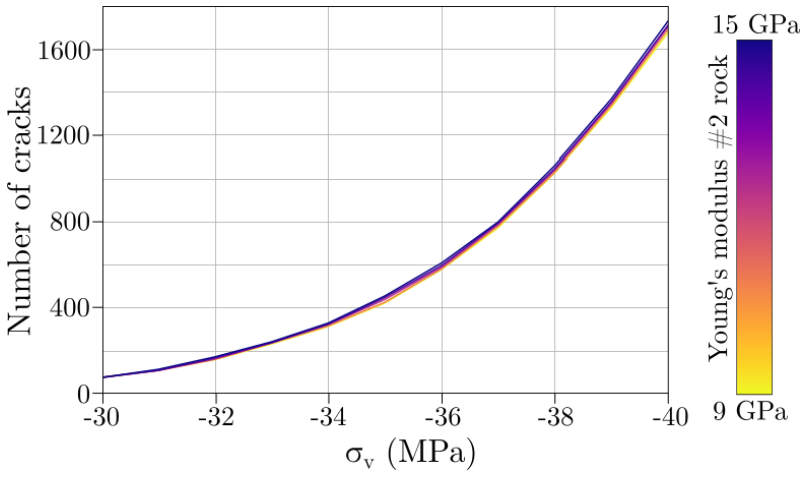

Figure 7. Amount of microfractures created in a homogeneous layer with low organic content rock #2 subjected to a compressive loading (kerogen maturation is not considered here). The horizontal stress is fixed for all simulations $\sigma_h = -11\ MPa$ while the vertical stress σ_v is increased. Five cases are shown for five different Young's moduli ranging from 6.8 GPa to 9.9 GPa (table 1).

3.4 Summary of the results for a non-layered rock

In this section, we discuss the two microfracturing mechanisms described in figure 1 taking place in a non-layered rock. The results show that:

- *(i)* the propagation of fluid induced microfractures is directly influenced by the far field stress: high deviatoric stresses tend to favor a propagation of the hydraulically driven fracture in the direction of the major principal stress.
- *(ii)* the overpressure needed to propagate fluid from a kerogen patch increases with the Young's modulus of the host medium as well as with the first stress invariant $I_{1,\#1}$ and the stress perpendicular to the kerogen patch.
- *(iii)* the amount of microfractures in the layers with low organic content increases with the first stress invariant $I_{1_{\#2}}$ and is independent of the Young's modulus of the host medium in the range of parameters tested here.

In the following section, we discuss how the layering of the rock material influences these microfracturing mechanisms. The main objective is to quantify the mechanisms and parameters which are most prone to create a three-dimensional fracture network that would facilitate fluid migration in a source rock.

4 Results for a layered rock

We investigate three different stress conditions: hydrostatic, normal faulting and reverse faulting regimes. For each scenario, twenty simulations were performed to consider every possible combinations of rock material properties given in table 1.

In each simulation, the amount of microfractures induced in the layer with low organic content is computed after the same amount of fluid was injected in the kerogen patches, as a proxy to quantify the ability of kerogen maturation to create a fracture network that could facilitate fluid migration. Results are depicted in figures 8, 10 and 12. Each figure contains two plots where the vertical and horizontal axes correspond to E_1 and E_2, the Young's moduli of the layers with high organic content #1, and low organic content #2, respectively. The background color maps represent the ratio σ_{h1}/σ_v in the layer with high organic content (left panel, equation 2), and the ratio σ_{h2}/σ_v in the layer with low organic content (right panel, equation 3) as those parameters are important to distinguish which mechanisms induce the fracturing (see section 3.4).

4.1 Hydrostatic loading condition: $\boldsymbol{\sigma_v = \sigma_h = -17.3\ MPa}$

Figure 8 shows the results of simulations performed under hydrostatic stress condition ($\sigma_v = \sigma_h = -17.3\ MPa$). Two different areas in the (E_1, E_2) plots can be distinguished.

Firstly the red shaded area in the left panel corresponds to a local stress condition where the main principal stress is vertical in the layers with high organic content. In this configuration, because of the deviatoric stress in the high organic content layer, the fluid induced microfractures emanating from the kerogen patches reorientate toward the vertical direction and propagate into the layers with low organic content, as shown in figure 9(a).

Secondly, the blue shaded area in the left panel corresponds to a local stress condition where the main principal stress is horizontal in the layers with high organic content (#1, red layers in figure 3). The microfractures appearing within the layers with low organic content are induced by the damaging mechanism related to the compression induced by the over-pressurization of the layer with high organic content #1 (mechanism 2 in figure 1(b)). As shown in figure 9(b), the hydraulically driven microfractures

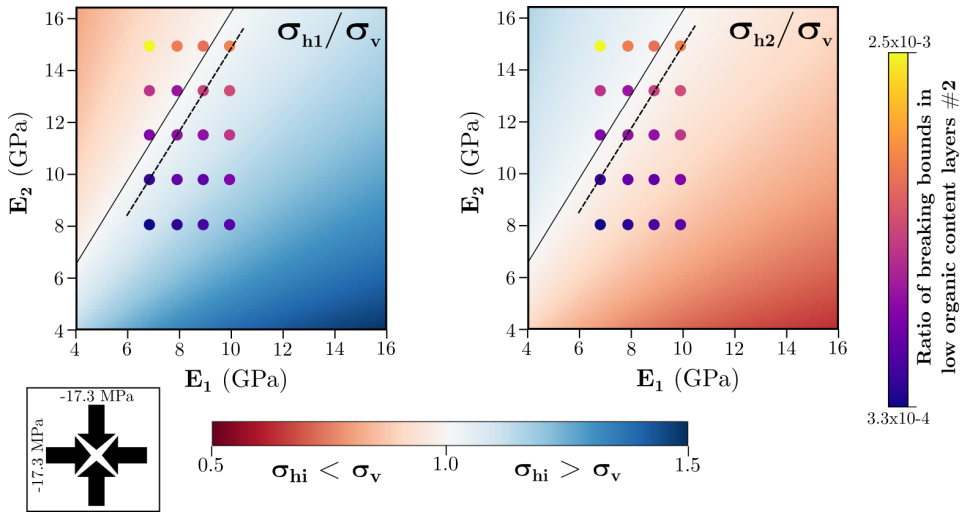

Figure 8. Amount of broken bonds induced in the layers with low organic content (#2, blue layers in figure 3): each dot corresponds to a simulation. The background colors correspond to the value of σ_{h1}/σ_v in the layers with high organic content (left) and to the value of σ_{h2}/σ_v in the layers with low organic content (right) computed using equations 2 and 3. $\sigma_h = \sigma_v = -17.3\ MPa$, and the total volume of injected fluid is the same for each case: 0.2 mm^3.

propagate horizontally inside the high organic content layers as the main principal stress is horizontal. The amount of damage in the layers with low organic content is correlated to the increase of pressure within the kerogen patches and to the initial confinement of the layer with low organic content ($I_{1,\#2}$).

The dashed line in figure 8 corresponds to a constant value of the first stress invariant in both layers. The increase of damage is linked to the increase of E_1 and E_2. As shown in figure 7, under a given confinement, the increase of E_2 has a negligible effect on the damaging processes. Therefore, the increase of damage is linked to the increase of E_1, which induces an increase of the overpressure (figure 6).

For a given value of E_1 (e.g., 10 GPa), the amount of microfractures increases when E_2 and $I_{1,\#2}$ increase and when $I_{1,\#1}$ decreases. A decrease of $I_{1,\#1}$ results in a decrease of the overpressure within the kerogen patches, which should lead to less damage in the layer with low organic content. However, this effect is counterbalanced by the increase of the confinement in the layers with low organic content $I_{1,\#2}$. As a consequence, the increase of confinement in the layers with low organic content $I_{1,\#2}$ has a stronger effect on damage development in those layers.

To conclude, under hydrostatic stress condition, the mechanism and amount of microfracturing in the layers with low organic content depends on the contrast of elastic properties between the layers. On the one hand, for an elastic contrast leading to a main principal stress oriented vertically in the layers with high organic content (reddish area in figure 8 left), microfracturing of the layers with low organic content is due to the reorientation of the fluid induced microfractures emanating from the kerogen patches in the direction perpendicular to the bedding. On the other hand, for an elastic contrast leading to a main principal stress oriented horizontally in the layers with high organic content (blueish area in figure 8 left), microfracturing of the layers with low organic content is due to the overpressure exerted by the two layers with high organic content that leads to compression induced damage. The parameters that have the strongest impact

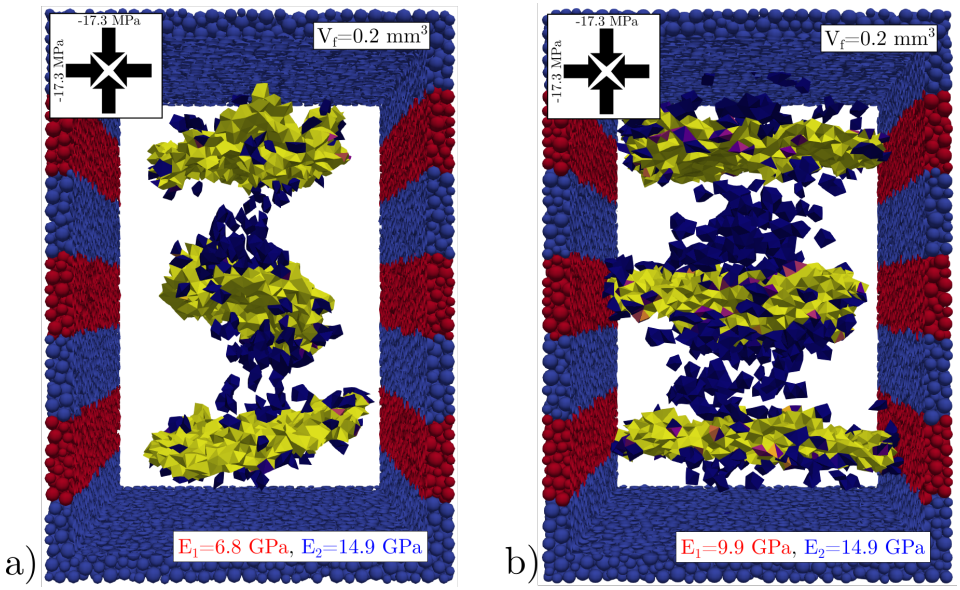

Figure 9. Three-dimensional views of the microfractures induced by kerogen maturation for two different sets of Young's moduli in the layers with high organic content (red) and low organic content (blue). The yellow cells correspond to microfractures filled with fluid and the dark blue cells to microfractures that do not contain fluid. The boundary stresses are $\sigma_h = \sigma_v = -17.3\ MPa$, and the total injected fluid volume is 0.2 mm^3. *(a)* Scenario with $E_1 = 6.8\ GPa$ in high organic content layers, and $E_2 = 14.9\ GPa$ in low organic content layers. *(b)* Scenario with $E_1 = 9.9\ GPa$ in high organic content layers, and $E_2 = 14.9\ GPa$ in low organic content layers.

on this damage are the initial confinement of the layer with low organic content ($I_{1,\#2}$, *(iii)*) and the Young's modulus of the layer with high organic content E_1.

4.2 Normal faulting loading condition: $\sigma_v = -30\ MPa, \sigma_h = -11\ MPa$

Figure 10 shows the results of simulations performed under normal faulting stress condition, with stress values similar to that measured at depth in the Draupne shale formation in the Norwegian Continental Shelf ($\sigma_v = -30\ MPa, \sigma_h = -11\ MPa$) (Zadeh et al., 2017).

Under such strong deviatoric stress condition (19 MPa), the main principal stress in both layer is vertical (figure 10). As shown in figure 10, the stress distribution over the range of elastic parameters investigated is similar for all cases (i.e., $\sigma_{h1}/\sigma_v \in [0.45, 0.5]$, $\sigma_{h2}/\sigma_v \in [0.26, 0.3]$). The amount of microfractures created within the low organic content layers after the injection of 0.22 mm^3 of fluid in the kerogen patches is significantly higher compared to the hydrostatic case (figure 8). As shown in figure 11, kerogen maturation induces the propagation of fluid driven microfractures toward the vertical direction which corresponds here to the direction of both the local and global major principal stress. Hence the main mechanism responsible for the microfracturing of the layers with low organic content in this configuration is the reorientation of the fluid induced microfractures emanating from kerogen patches into these layers.

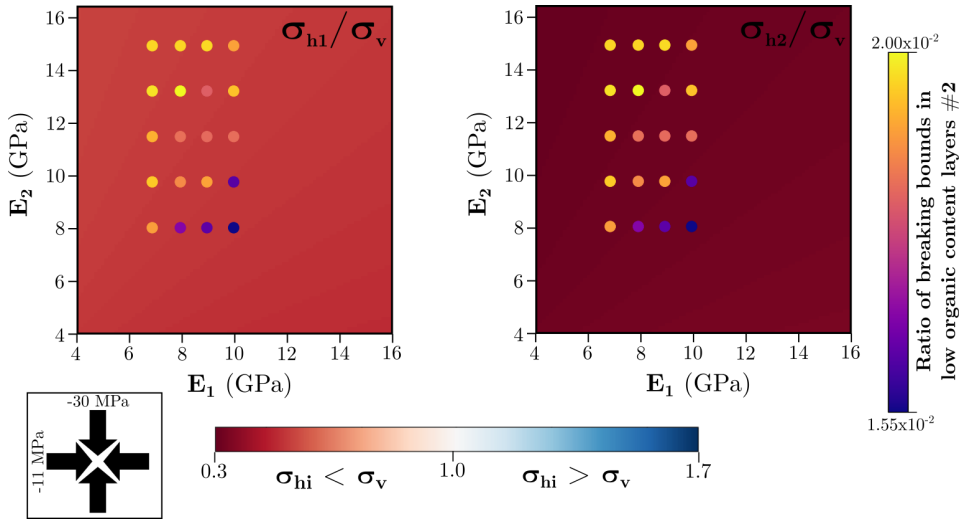

Figure 10. Amount of broken bonds induced in the layers with low organic content (#2, blue layers in figure 3): each dot corresponds to a simulation. The background colors correspond to the value of σ_{h1}/σ_v in the layers with high organic content (left) and to the value of σ_{h2}/σ_v in the layers with low organic content (right) computed using equations 2 and 3. $\sigma_h = -11\ MPa$, $\sigma_v = -30\ MPa$, and the total volume of injected fluid is the same for each case: 0.22 mm^3.

4.3 Reverse faulting loading condition: $\sigma_v = -10\ MPa, \sigma_h = -21\ MPa$

Figure 12 shows the results from simulations performed under reverse faulting stress condition ($\sigma_v = -10\ MPa, \sigma_h = -21\ MPa$). In this case, the stress field in both layers with high and low organic content is dominated by the horizontal stress component ($\sigma_{hi}/\sigma_v > 1$). Maturation of kerogen patches induces the propagation of fluid driven microfractures along the horizontal direction in all configurations, as shown in figure 13. The amount of microfractures induced by compaction within the low organic content lay-

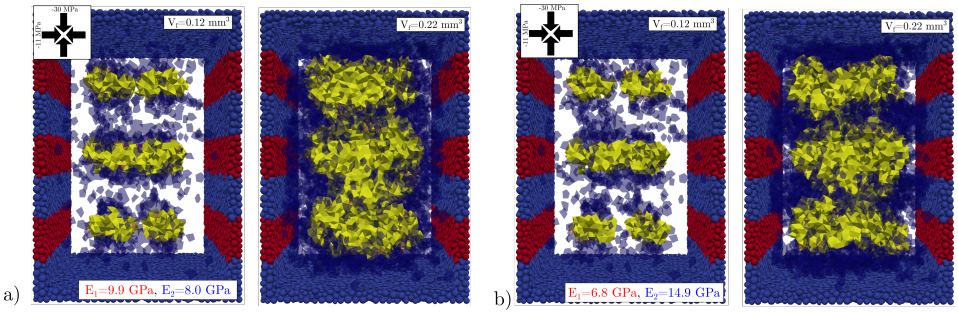

Figure 11. Three-dimensional view of microfractures induced by kerogen maturation for two different sets of Young's moduli in tje layers with high organic content (red) and low organic content (blue). The yellow cells corresponds to microfractures filled with fluid and the dark blue cells to microfractures that do not contain fluid. The boundary stresses are $\sigma_h = -11\ MPa$ and $\sigma_v = -30\ MPa$. *(a)* Scenario with $E_1 = 9.9\ GPa$ in the layers with high organic content, and $E_2 = 8.0\ GPa$ in the layers with low organic content for two different volumes of fluid injected into the kerogen patches (0.12 mm^3 and 0.22 mm^3). *(b)* Scenario with $E_1 = 6.8\ GPa$ in the high organic content layers, and $E_2 = 14.9\ GPa$ in low organic content layers for two different volumes of fluid injected into the kerogen patches (0.12 mm^3 and 0.22 mm^3).

ers is low compared to the normal faulting and hydrostatic stress conditions (figures 10 and 8).

Under this reverse faulting regime, damage of the low organic content layers increases with the initial confinement of these layers ($I_{1,\#2}$) as shown in figures 12 and 13 *(iii)*. For a given stress condition (σ_{hi}/σ_v, dashed line figure 12), the amount of crack increases with the Young's modulus of the high organic content layers, as expected from the fluid overpressure increases due to the high Young's modulus of high organic content layers *(ii)* (figure 6). Conversely, the initial confinement exerted on the high organic content layers ($I_{1,\#1}$) does not have a significant impact on the damage, as on figure 12 where the amount of crack decreases with the increase of $I_{1,\#1}$. This result indicates that the value of $I_{1,\#1}$ as a minor effect on the fracturing of the low organic content layers, compared to their initial confinement $I_{1,\#2}$ and to the effect of the Young's modulus of the high organic content layer E_1. These conclusions are similar to the ones for the hydrostatic case.

5 Discussion

Microfractures induced by kerogen maturation in shales have been proposed as a possible mechanism to increase shale permeability and enhance fluid migration from source to reservoir rocks during primary migration (Pelet & Tissot, 1971; Vernik, 1994; Teixeira et al., 2017). For a homogeneous, elastic and isotropic shale, Teixeira et al. (2017) have shown that microfracturing under strong deviatoric stress leads to the reorientation of the fluid induced microfractures emanating from kerogen patches toward the principal stress direction, allowing the fluid to migrate toward the reservoir.

Here, we specifically study the effect of structural layering in shales on the development of microfractures induced by kerogen maturation. Layering in shales comes from the sedimentary processes of shale formation through successive deposition of typically sandy and clayey layers in a sedimentary basin. Those layers can present different elastic properties and a variety of thicknesses (Li et al., 2017). We used coupled hydro-mechanical simulations to investigate the effect of this layering on microfracture development and

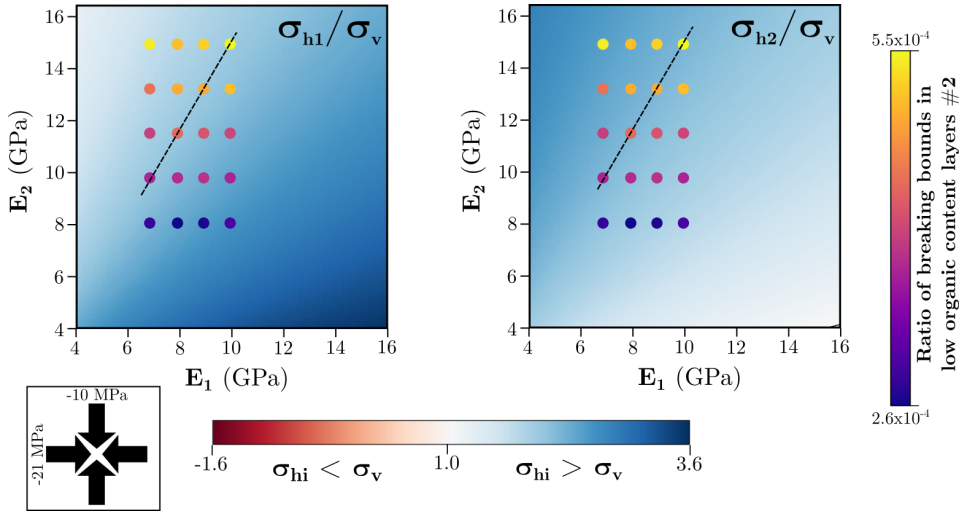

Figure 12. Amount of broken bonds induced in the layers with low organic content (#2, blue layers in figure 3): each dot corresponds to a simulation. The background colors correspond to the value of σ_{h1}/σ_v in the layers with high organic content (left) and to the value of σ_{h2}/σ_v in the layers with low organic content (right) computed using equations 2 and 3. $\sigma_h = -21\ MPa$, $\sigma_v = -10\ MPa$, and the total injected fluid volume is the same for each case: 0.2 mm^3.

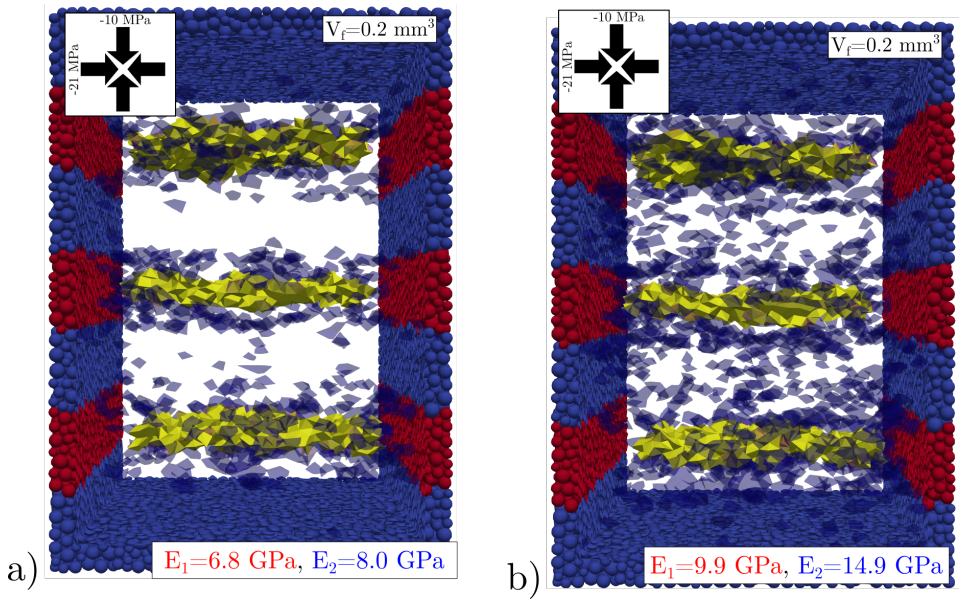

Figure 13. Three-dimensional view of microfractures induced by kerogen maturation for two different sets of Young's moduli in the layers with high organic content (red) and low organic content (blue). The yellow cells correspond to microfractures filled with fluid and the dark blue cells to microfractures that do not contain fluid. The boundary stresses are $\sigma_h = -21\ MPa$ and $\sigma_v = -10\ MPa$, and the total injected fluid volume is 0.2 mm^3. *(a)* Scenario with $E_1 = 6.8\ GPa$ in the high organic content layers, and $E_2 = 8.0\ GPa$ in the low organic content layers. *(b)* Scenario with $E_1 = 9.9\ GPa$ in the high organic content layers, and $E_2 = 14.9\ GPa$ in the low organic content layers.

fluid migration in shales. Relevant mechanical parameters (Young's modulus, Poisson's ratio, strength) were chosen from borehole and core data from the Draupne shale formation in the Norwegian Continental Shelf (Mondol, 2019) (table 1). Three different stress boundary conditions were investigated in order to cover a large range of stresses conditions encountered in sedimentary basins, from normal faulting, such as for the stress state measured in the Draupne shale ($\sigma_v = -30\ MPa, \sigma_h = -11\ MPa$), to reverse faulting ($\sigma_h > \sigma_v$) and hydrostatic loading ($\sigma_h = \sigma_v$).

Under normal faulting stress condition, as in the Draupne shale formation, kerogen maturation induces fluid production which leads to the fracturing of all the shale layers due to the propagation and reorientation of hydraulically driven fractures emanating from the kerogen patches (figures 10 and 11). The distribution of stress due to layering has a minor effect on the fracturing process because the initial deviatoric stress is large enough. Under such configuration, the reorientation of the fluid driven microfractures emanating from kerogen patches (mechanism 1 in figure 1b) creates preferential fluid pathways in the vertical direction which facilitates fluid migration toward the reservoir.

Under hydrostatic stress condition, the contrast in elastic parameters between the layers forming the rock has a greater impact on the microfracturing mechanisms. Two different scenarios are possible. Under such loading conditions, even if the stress is hydrostatic at the macroscopic scale, a deviatoric component exists in each layer because of the elastic contrast between layers (e.g., figure 4). First, if the vertical stress is higher than the horizontal stress in the layers with high organic content ($\sigma_{h1}/\sigma_v < 1$, red areas in figure 8 left), the fluid driven microfractures emanating from the kerogen patches reorientate toward the vertical direction and fracture the layers with low organic content (figure 9 left). On the other hand, if the horizontal stress is greater than the vertical stress in the layers with high organic content, the fluid driven microfractures emanating from the kerogen patches propagate horizontally and remain contained within the layer with high organic content (figure 9 right). In this case, damage is produced in the layers with low organic content due to local compressive stress increase induced by the pressure buildup caused by kerogen maturation. The main parameter controlling this damaging process is the initial confinement of the layer with low organic content, ($I_{1,\#2}$). The higher the initial confinement is, the more efficient this damaging process will be. The initial confinement is controlled by the elastic contrast between the layers and the external stress conditions as expressed by equation 3. The overpressure needed for hydraulically driven fractures to propagate from the kerogen patches can vary due to the initial confinement or the value of the Young's modulus of the layers with high organic content, ($I_{1,\#1}$) (figure 6).

The behavior of the layered rock under reverse faulting stress condition is similar to the hydrostatic case when the horizontal stress is higher than the vertical stress in the layers with high organic content, ($\sigma_{h1} > \sigma_v$). When the horizontal stress corresponds to the main principal stress in both layers with high or low organic content (figure 12), fluid driven microfractures produced by kerogen maturation propagate in the horizontal plane, parallel to the bedding (figure 13). Damage within layers with low organic content is due to the compression of these layers by the maturation induced pressure buildup in the surrounding organic-rich layers. The overpressures under reverse faulting condition is significantly lower than the overpressure under hydrostatic condition (figure 6) due to the lower projected stress on the kerogen patches. Hence, less microfractures are induce in the layers with low organic content under reverse faulting condition (figure 12). In the range of elastic parameters investigated here, the variation in the amount of microcracks formed is correlated to the increase of stress confinement in the layers with low organic content, ($I_{1,\#2}$).

From those three different stress scenarios, the main conclusions are summarized in figure 14 which displays the different stress regimes admissible in the layers with low

or high organic content. The blue color shades correspond to macroscopic reverse faulting stress regimes and the red color shades correspond to normal faulting regimes. Two different domains can be defined: *(1)* $\sigma_v > \sigma_{h1}$, where the reorientation of the hydraulically driven microfractures emanating from kerogen patches is the main fracturing mechanism in layers with low organic content. *(2)* $\sigma_v < \sigma_{h1}$, where hydraulically driven microfractures emanating from kerogen patches propagate along the bedding, within the layers with high organic content. In such case, the mechanism creating damage in the layer with low organic content is the compression of this layer due to the overpressurization of the kerogen patches present in the organic-rich layers located below and above. For given external stress conditions, damage within the layers with low organic content is mainly controlled by the initial confinement $I_{1,\#2}$. If the initial vertical stress σ_v remains constant, the increase of $I_{1,\#2}$ is related to the increase of σ_{h2}/σ_v. A second parameter controlling damage in the layers with low organic content is the Young's modulus of the layers with high organic content, as shown in figures 8 and 12 (dashed lines). The Young's modulus has a strong influence on the maximum overpressure needed for hydraulically driven fractures to propagate as a result of kerogen maturation (figure 6). This overpressure controls the damage induced within the layer with low organic content.

Laboratory studies on immature shale samples have been performed and fracturing induced by kerogen maturation was visualized using either scanning electron microscopy (Allan et al., 2014) or time-lapse synchrotron X-ray microtomography (Kobchenko et al., 2011; Panahi et al., 2013). Those experiments were carried out without external stress applied and showed hydraulic fracture propagation along the bedding plane, which corresponds to the preferential direction of the penny shaped kerogen patches. Teixeira et al. (2017) presented X-ray microtomography images with differential stress applied during maturation and highlighted the formation of vertical hydraulic driven fracture,s as confirmed by our simulations. In those simulations, damage in low organic content layers is shown to connect high organic content layers through channels, creating a three-dimensional fluid pathways for primary migration. These experimental results are consistent with the simulation presented in this paper.

6 Conclusion

The influence of structural layering in shales on fluid expulsion during hydrocarbon formation is investigated for different stress conditions using hydro-mechanically coupled simulations. The nucleation and growth of microfractures induces an increase of permeability which allows primary migration from the source rock to the reservoir. Two main mechanisms of permeability enhancement are identified (figure 1), both related to the increase of fluid pressure due to kerogen maturation. The main results are displayed in figure 14 and can be summarized as follows:

1. Hydraulically driven microfractures form due to local fluid overpressure induced by kerogen maturation. They emanate from the kerogen patches and may rotate in the direction of the local main principal stress during their propagation. Under normal faulting stress conditions, this direction is vertical and flow pathways connected in three dimensions may form (mechanism 1, black microfractures in figure 1). This process is directly controlled by the state of stress in the layers with high organic content. If the vertical stress is higher than the horizontal stress $\sigma_v > \sigma_{h1}$, these maturation induced fractures propagate toward the vertical direction. This configuration is likely to be reached under normal faulting stress conditions but can also be reached in some reverse faulting stress conditions (figure 14 where $\sigma_{h1}/\sigma_v < 1$).
2. If the horizontal stress is larger than the vertical stress in the layers with high organic content, hydraulically driven microfracture caused by kerogen maturation

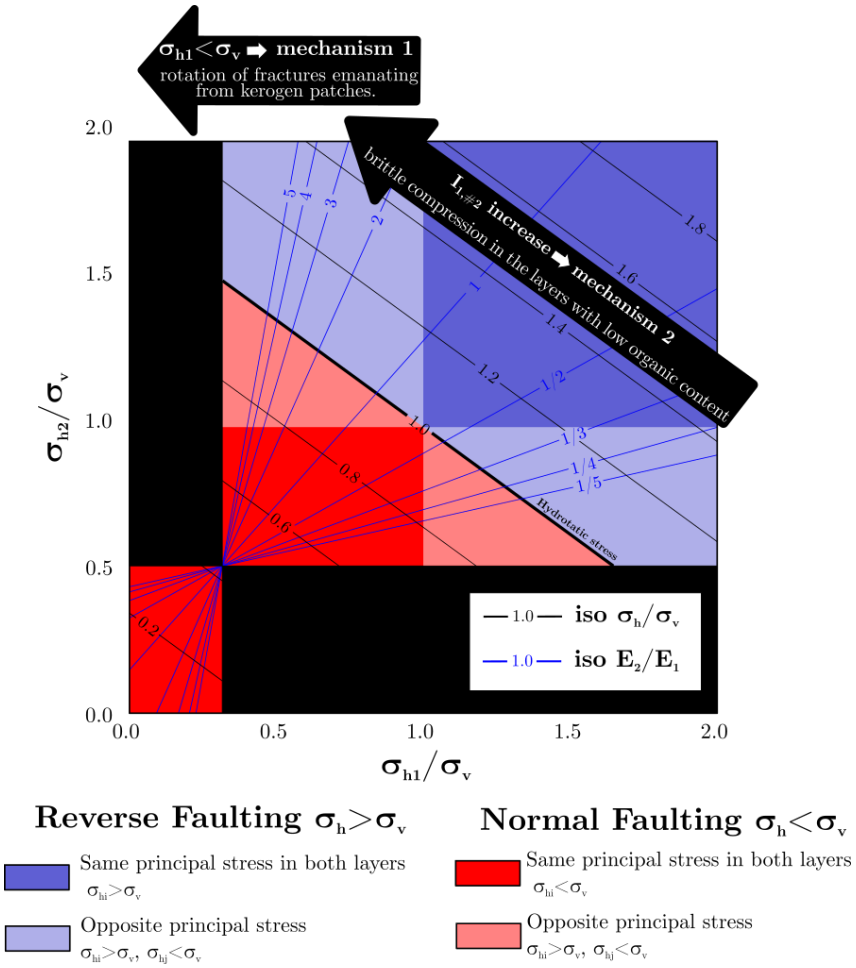

Figure 14. Summary of the local stress distributions in the layers with low (σ_{h2}/σ_v) and high (σ_{h2}/σ_v) organic content as functions of their elastic properties and the far-field stress. These stress conditions control the mechanisms responsible for microfracturing of the layers with low organic content. This figure is built from equations 2 and 3, for a given Poisson's ratio ($\nu_1 = 0.34, \nu_2 = 0.24$) and a given proportion of high organic content rock ($q_1 = 3/7$), corresponding to the simulations.

propagate within these layers. Then, damage in the layers with low organic content is caused by the compression of those layers induced by the pressure buildup of the high organic content layers (mechanism 2, white microfractures in figure 1. The two main parameters controlling this fracturing process are the initial confinement of the layers with low organic content ($I_{2,\#2}$), which results from the elastic contrast between the layers, and the Young's modulus of the layers with high organic content.

Appendix A State of stress in a layered linear elastic material

A layered rock made of two linear elastic isotropic materials is considered. Both materials are characterized by a Young's modulus E_i, a Poisson's ratio ν_i and a volume fraction q_i (with $q_1 + q_2 = 1$), as shown in figure A1. The applied loading is assumed to be transverse isotropic, with (σ_v, σ_h) respectively perpendicular and parallel to the layers (see Figure A1). In this configuration the vertical stress, along z-axis, is the same in both layer and equal to σ_v.

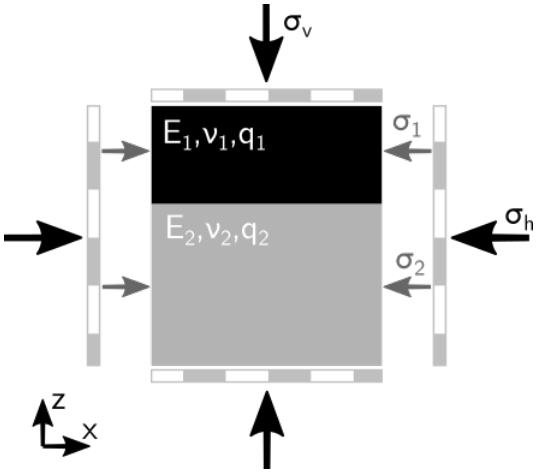

Figure A1. Schematic representation of a layered rock with imposed elastic parameters and loading conditions.

Applying Hooke's law on an elastic isotropic material (equation 1), we can project the strain tensor for both material on the $\vec{x}$ axis. The strain along the $\vec{x}$ axis is geometrically constrained to be the same for both materials and is noted ε_t.

$$(Eq\ 1)_{\#1}.\vec{x} \Leftrightarrow \varepsilon_t = \frac{1+\nu_1}{E1}\sigma_{h1} - \frac{\nu_1}{E_1}\left(2\sigma_{h1} + \sigma_v\right) \tag{A1}$$

$$(Eq\ 1)_{\#2}.\vec{x} \Leftrightarrow \varepsilon_t = \frac{1+\nu_2}{E2}\sigma_{h2} - \frac{\nu_2}{E_2}\left(2\sigma_{h2} + \sigma_v\right) \tag{A2}$$

and σ_{h1} and σ_{h2} are related to σ_v through:

$$q_1\sigma_{h1} + (1-q_1)\sigma_{h2} = \sigma_v \tag{A3}$$

Solving the set of equations A4 and introducing the parameter $P_\sigma = \frac{\sigma_h}{\sigma_v}$, it is possible to calculate analytically $\frac{\sigma_{hi}}{\sigma_v}$ from six known parameters: $\frac{\sigma_{hi}}{\sigma_v} = g(E_i, \nu_i, P_\sigma, q_1)$ (Equations A5 and A6).

$$\begin{cases} (Eq.\ A1) - (Eq.\ A2) \Leftrightarrow f(E_i, \nu_i, \sigma_i, \sigma_v, q_1) \\ \sigma_h = q_1\sigma_{h1} + (1+q_1)\sigma_{h2} \end{cases} \tag{A4}$$

$$\frac{\sigma_{h1}}{\sigma_v} = \frac{E_1 P_\sigma\,(\nu_2 - 1) + (E_1\nu_2 - E2\nu1)\,(1-q1)}{E_1 q_1(\nu_2 - 1) + E2(1-q_1)(\nu_1 - 1)} \tag{A5}$$

$$\frac{\sigma_{h2}}{\sigma_v} = \frac{E_2 P_\sigma\,(\nu_1 - 1) + (E_2\nu_1 - E1\nu2)\,q1}{E_1 q_1(\nu_2 - 1) + E2(1-q_1)(\nu_1 - 1)} \tag{A6}$$

Notation

$\boldsymbol{E_1}$, Young's modulus of material #1
$\boldsymbol{\nu_1}$ Poisson's ratio of material #1
q1 volume fraction of material #1
$\boldsymbol{E_2}$, Young's modulus of material #2
$\boldsymbol{\nu_2}$ Poisson's ratio of material #2
q2 volume fraction of material #2
$\boldsymbol{\sigma_v}$ applied vertical stress
$\boldsymbol{\sigma_h}$ applied horizontal stress
$\boldsymbol{\sigma_{h1}}$ horizontal stress in layers with high organic content
$\boldsymbol{\sigma_{h2}}$ horizontal stress in layers with low organic content
$\boldsymbol{P_\sigma}$ $= \frac{\sigma_h}{\sigma_v}$
$\boldsymbol{I_1}$ $= trace\,(\bar{\bar{\sigma}})$, macroscopic first stress invariant
$\boldsymbol{I_{1,\#1}}$ first stress invariant in layers with high organic content
$\boldsymbol{I_{1,\#2}}$ first stress invariant in layers with low organic content
$\boldsymbol{V_f}$ injected fluid volume

Acknowledgments

The Research Council of Norway funded this study (Petromaks 2 programme, grant 267775). Numerical simulations were performed with the open source code Yade (Kozicki & Donzé, 2008, 2009; Šmilauer et al., 2015). The scripts and data used for the simulations and to produce the figures will be made available on Github upon acceptance of this article (`https://github.com/ThomasChauve/JGRPaper_layering_shale`).

References

Allan, A., Vanorio, T., & Dahl, J. (2014). Pyrolysis-induced P-wave velocity anisotropy in organic-rich shales. *Geophysics*, *79*(2), D41–D53. doi: 10.1190/geo2013-0254.1

Fan, Z. Q., Jin, Z.-H., & Johnson, S. E. (2012). Modelling petroleum migration through microcrack propagation in transversely isotropic source rocks. *Geophysical Journal International*, *190*(1), 179–187. doi: 10.1111/j.1365-246X.2012.05516.x

Gale, J. F. W., Laubach, S. E., Olson, J. E., Eichhubl, P., & Fall, A. (2014). Natural fractures in shale: A review and new observations. *AAPG Bulletin*, *98*(11), 2165–2216. doi: 10.1306/08121413151

Gunzburger, Y., & Magnenet, V. (2014). Stress inversion and basement-cover stress transmission across weak layers in the Paris basin, France. *Tectonophysics*, *617*, 44–57. doi: 10.1016/j.tecto.2014.01.016

Horsrud, P., Sønstebø, E. F., & Bøe, R. (1998). Mechanical and petrophysical properties of North Sea shales. *International Journal of Rock Mechanics and Mining Sciences*, *35*(8), 1009–1020. doi: 10.1016/S0148-9062(98)00162-4

Jin, Z., Johnson, S. E., & Fan, Z. Q. (2010). Subcritical propagation and coalescence of oil-filled cracks: Getting the oil out of low-permeability source rocks. *Geophysical Research Letters*, *37*, L01305. doi: 10.1029/2009GL041576

Kalani, M., Jahren, J., Mondol, N. H., & Faleide, J. I. (2015). Petrophysical implications of source rock microfracturing. *International Journal of Coal Geology*, *143*, 43–67. doi: 10.1016/j.coal.2015.03.009

Kobchenko, M., Panahi, H., Renard, F., Dysthe, D. K., Malthe-Sørenssen, A., Mazzini, A., ... Meakin, P. (2011). 4d imaging of fracturing in organic-rich shales during heating. *Journal of Geophysical Research: Solid Earth*, *116*(B12), B12201. doi: 10.1029/2011JB008565

Kozicki, J., & Donzé, F. (2009). YADE-OPEN DEM: an open-source software using a discrete element method to simulate granular material. *Engineering Computations*, *26*(7), 786–805. doi: 10.1108/02644400910985170

Kozicki, J., & Donzé, F. V. (2008). A new open-source software developed for numerical simulations using discrete modeling methods. *Computer Methods in Applied Mechanics and Engineering*, *197*(49), 4429–4443. doi: 10.1016/j.cma.2008.05.023

Li, L., Huang, B., Tan, Y., Deng, X., Li, Y., & Zheng, H. (2017). Geometric Heterogeneity of Continental Shale in the Yanchang Formation, Southern Ordos Basin, China. *Scientific Reports*, *7*(1). doi: 10.1038/s41598-017-05144-z

Mondol, N. H. (2019). Geomechanical and Seismic Behaviors of Draupne Shale: A Case Study from the Central North Sea. In (Vol. 2019, pp. 1–5). European Association of Geoscientists & Engineers. doi: 10.3997/2214-4609.201901599

Ougier-Simonin, A., Renard, F., Boehm, C., & Vidal-Gilbert, S. (2016). Microfracturing and microporosity in shales. *Earth-Science Reviews*, *162*, 198–226. doi: 10.1016/j.earscirev.2016.09.006

Panahi, H., Kobchenko, M., Meakin, P., Dysthe, D. K., & Renard, F. (2018). In-situ imaging of fracture development during maturation of an organic-rich shale: Effects of heating rate and confinement. *Marine and Petroleum Geology*, *95*, 314–327. doi: 10.1016/j.marpetgeo.2018.05.002

Panahi, H., Kobchenko, M., Renard, F., Mazzini, A., Scheibert, J., Dysthe, D. K., ... Meakin, P. (2013). A 4d synchrotron X-ray tomography study of the formation of hydrocarbon migration pathways in heated organic-rich shale. *SPE Journal*, *18*(2), 366–377. doi: 10.2118/162939-PA

Papachristos, E., Donzé, F. V., Chareyre, B., Scholtès, L., & Pourpak, H. (2016). 3d Hydro-Mechanical Modeling of Multiple Injections. American Rock Mechanics Association.

Pelet, R., & Tissot, B. (1971). Nouvelles Données sur les Mécanismes de Genèse et de Migration du Pétrole Simulation Mathématique et Application à la Prospection. World Petroleum Congress.

Teixeira, M. G., Donzé, F., Renard, F., Panahi, H., Papachristos, E., & Scholtès, L. (2017). Microfracturing during primary migration in shales. *Tectonophysics*, *694*, 268–279. doi: 10.1016/j.tecto.2016.11.010

Valès, F., Nguyen Minh, D., Gharbi, H., & Rejeb, A. (2004). Experimental study of the influence of the degree of saturation on physical and mechanical properties in Tournemire shale (France). *Applied Clay Science*, *26*(1), 197–207. doi: 10.1016/j.clay.2003.12.032

Vernik, L. (1994). Hydrocarbon-generation-induced microcracking of source rocks. *Geophysics*, *59*(4), 555–563. doi: 10.1190/1.1443616

Zadeh, M. K., Mondol, N. H., & Jahren, J. (2017). Velocity anisotropy of Upper Jurassic organic-rich shales, Norwegian Continental Shelf Anisotropy of organic-rich shales. *Geophysics*, *82*(2), C61–C75. doi: 10.1190/

geo2016-0035.1

Zhang, Y., & Zhang, J. (2017). Lithology-dependent minimum horizontal stress and in-situ stress estimate. *Tectonophysics*, *703-704*, 1–8. doi: 10.1016/j.tecto.2017.03.002

Zoback, M. D. (2007). *Reservoir Geomechanics*. Cambridge: Cambridge University Press. doi: 10.1017/CBO9780511586477

Šmilauer, V., Catalano, E., Chareyre, B., Dorofeenko, S., Duriez, J., Dyck, N., ... Yuan, C. (2015). Reference Manual. Zenodo. doi: 10.5281/zenodo.34045